Multiscale deformation processes during cold sintering of nanovaterite compacts

Matthias Haug, Florian Bouville, Jerome Adrien, Anne Bonnin, Éric Maire, Andre R. Studart

Multiscale deformation processes during cold sintering of nanovaterite compacts

Matthias Haug [1], Florian Bouville [1+], Jérome Adrien [2], Anne Bonnin [3], Eric Maire [2], André R. Studart [1]

[1] Complex Materials, Department of Materials, ETH Zürich, 8093 Zürich, Switzerland

[+] current affiliation: CASC, Imperial College London, United Kongdom

[2] MATEIS, INSA, Université de Lyon, France

[3] Paul Scherrer Institut, PSI, Villigen, Switzerland

Abstract

Cold sintering is a promising route towards the manufacturing of dense ceramics at mild processing conditions, but our poor understanding of the process has prevented the wider spread of this attractive densification approach. Using nanovaterite powders with well-defined multiscale morphology, we perform *in-situ* X-Ray tomography on compacts subjected to controlled mechanical load and quantify the multiscale deformation processes responsible for the water-assisted cold sintering of this powder with the help of instrumented indentation experiments at the micro- and nano-scale. Our results reveal the crucial effect of water in promoting the macroscopic densification process and highlight the dominant role of the nanoparticle network inside agglomerates in controlling the cold sintering of compacts at high mechanical loads. By providing new insights into the deformation processes responsible for the densification effect, this study can potentially guide the discovery of novel chemical compositions and particle morphologies that can be more easily densified through room-temperature cold sintering with water.

Keywords: densification, pressing, calcium carbonate, indentation, X-Ray tomography

1. Introduction

Cold sintering of powder compacts is a well-known geological process leading to rock formation in nature [1, 2] and has recently been explored for the fabrication of advanced ceramics for electronic and structural applications. [3-6] In geology, the densification of granular materials through pressure solution creep is an important mechanism underlying the formation and transformations of sedimentary rocks. [2, 7] Pressure solution creep is a cold sintering process that enables the transport of atoms from inter-particle contacts to pore walls in a similar fashion to the conventional densification and sintering of ceramics at high temperatures. As far as ceramics are concerned, cold sintering offers an attractive sustainable pathway for the fabrication of stiff and strong functional materials in aqueous environment at much lower temperature compared to standard sintering conditions. [3] Given its relevance to such

a broad spectrum of materials and research fields, cold sintering processes have been intensively studied by the geology and materials science communities in recent years. [3, 5, 6, 8]

The densification of powder compacts through cold sintering has been demonstrated for a wide range of chemical compositions and processing conditions. [9] While low-temperature dissolution and reprecipitation processes have long been known to enable the pressure-assisted densification of sedimentary rocks, [10] the possibility to cold sinter salts, phosphates, carbonates and oxide ceramics featuring much lower solubility in water has only recently been evidenced by materials scientists. [3-11] Early works exploring this attractive processing route focused on the cold sintering of hydroxyapatite and lithium molybdate powders under temperatures and pressures in the range of 20-250 °C and 50-130 MPa. [5, 11] Other studies revealed that similar pressures and temperatures can be used to densify ZnO powder compacts through hydrothermal processes. [4, 8] More recent research has shown that hydrothermal conditions can be extended to cold sinter an impressive range of chemical compositions, including various simple and complex oxides, carbonates and salts. [6] Inspired by the densification of carbonates in geological formations, we have demonstrated that the cold sintering of nanovaterite powder is possible even at room temperature by compaction of the powder with water under pressures in the range 10 – 800 MPa. [3] Despite these several successful demonstrations of cold sintered materials, the microstructural deformation processes underlying the densification of such powders remain poorly understood. In particular, the morphology of the initial powders is expected to play an important role on the room-temperature sintering of nanovaterite with water, but its effect on the deformation processes within the compact under pressure has not yet been systematically studied.

Three-dimensional X-Ray tomography is a powerful *in-situ* experimental technique to assess the deformation processes within materials subjected to mechanical loading. [12] This has allowed for the space and time-resolved quantification of the porosity of metal powder compacts used in powder metallurgy, [13, 14] the mapping of strains and defects developed during the mechanical deformation of metals, [15] and the analysis of matter transport mechanisms during high-temperature sintering of glass and oxide-based composites. [16, 17] Synchrotron based tomography has also been used to observe particle morphology changes during pressure solution creep of 100µm sodium chloride particles. [18] Besides *in-situ* tomography, instrumented micro- and nano-indentation has also been extensively employed to quantify the mechanical response and deformation processes in consolidated or pressed materials. [19] By measuring the creep response of specimens tested with different indenter sizes, this technique provides a means to probe deformation processes at different length scales. [20] The combined use of such imaging and mechanical characterization tools should therefore be a powerful approach to study cold sintering phenomenon in powder compacts.

Here, we apply *in-situ* X-Ray tomography and instrumented mechanical indentation to investigate the deformation processes at play during the room-temperature cold sintering of nanovaterite under pressure with water. Because the investigated vaterite powder displays a multiscale morphology comprising agglomerates of interconnected nanoparticles, special attention is given to the quantification of the deformation mechanisms operating at different length scales. To this end, the displacement of vaterite agglomerates during uniaxial pressing is first observed through spatially- and time-resolved

imaging using a custom-made mechanical testing setup positioned in a synchrotron beamline. Digital volume correlation is then applied on the reconstructed volumes to map local deformation of the compacts during stress relaxation experiments. This is later complemented with micro- and nano-indentation analysis to understand the role of the multiscale powder morphology on the cold sintering process. On the basis of these experiments, we finally propose a model to describe the deformation processes responsible for the water-assisted densification of nanovaterite powder under compression.

2. Experimental

2.1. Synthesis of nanovaterite particles

Nanovaterite particles were synthesized following a procedure published in the literature. [21] Briefly, 2 mol L^{-1} aqueous solutions of sodium carbonate (Na_2CO_3, Sigma-Aldrich, Germany) and of calcium chloride (calcium chloride dihydrate, $CaCl_2 \cdot 2H_2O$, Merck, Germany) were prepared with deionized (DI) water. 16 ml of each solution were diluted with 80 ml of DI water, resulting in a solute concentration of 0.33 mol L^{-1}. The solutions were mixed well for a few minutes and the precipitated vaterite particles were immediately separated from the water by centrifugation at 4500 rpm for 5 min. The particles were then re-dispersed and washed twice with ethanol (94% denaturated with toluene, Alcosuisse) before drying in an oven at 60 °C overnight and at 120 °C for another 24 h. One batch typically resulted in 3 g of $CaCO_3$ particles.

2.2. Characterization of the nanovaterite particles

The crystallographic phase of the particles was characterized by X-Ray powder diffraction (XRD, Panalytical X'Pert PRO MPD, Netherlands) using a Cu anode (generation voltage 40 kV, tube current 45 mA) and a monochromator. The time per step was set to 600 s and the step size to 0.0167° while varying the 2θ angle from 10° to 70°. The morphology of the particles was analyzed by scanning electron microscopy (SEM, Zeiss, LEO 1530, Zeiss, Germany). Prior to acquiring the images, the particles were coated with a 5 nm layer of Pt in order to make the samples electrically conductive.

2.3. Tomography set up

To build the custom-made pressing die and punch, a round single boron tube (outer diameter: 1.27 mm, inner diameter: 0.50 mm, length: 50 mm) and a solid rod (diameter: 0.50 mm, length: 50 mm) made from alumina (99.8%) were acquired from Ortech Inc. (Sacramento, Ca, USA). The tube was cut into small pieces, each 6 mm long with a wire saw. For the lower part of the pressing die the inner solid rod was carefully broken to reach 2 mm inside the tube. The upper part of the pressing tool was broken to remain 2 mm outside the die in the absence of powder in the cavity. The lower part of the pressing tool together with the outer tube was glued onto a metallic base plate using super glue (UHU, Superflex Gel).

For the tomography experiments, the particles were mixed with water to reach a liquid-to-powder (L/P) mass ratio of 0.25. After filling the cavity with either the prepared wet powder or dry powder, the pressing tool was taped to better accommodate the nanovaterite particles. The pressing punch was inserted and

used to slightly compact the powder before placing the setup in a custom-made tensile/compression rig positioned at the beam line. More details on the rig can be found in previous work by Maire *et al* [15] . To ensure that the water would not evaporate from the wet sample during the measurement, a drop of water was placed on top of the pressing tool before the series of scans started.

The rig was used to increase the force acting on the powder while a constant displacement rate was applied. Once the desired forces of 20 N (100 MPa) or 100 N (500 MPa) were reached the tester was stopped manually. Force and displacement data were recorded at a frequency of 2 Hz. Scans were then acquired at constant displacement after 2, 5, 10, 30 and 30 min to track the movement of the particles over time.

A PCO-Edge 5.5 Camera was used in a Optic Peter MB optical microscope at a magnification of 4 resulting in a lateral pixel size of 0.165 in the projections. The exposure time was 30 ms per projection with no delay time. The following scanning settings were used: 601 projections, 20 darks and 40 flats with no inter-flats. The sample was rotated by a total amount of 180°. The dimension in pixels of the projections was 2560x2160 pixels. We used a paganin phase retrieval algorithm and adjusted the rotation center. For the reconstruction, the Gridrec algorithm with the ramp filter was employed. The reconstruction was stored slice by slice as .tif files coded on 8 bits.

2.4. Digital volume correlation

The slices were scaled down by a factor of 0.25 in all 3 dimensions by applying the ‘scale’ command from Fiji [22] to obtain a stack of processable size. Averaging was used during downsizing. Images from the different time steps were loaded into one hyper stack. A region of interest in the lower part of the 3D volume was selected to apply the Fiji plugin ‘correct 3D drift’ to correct for the drift between the different time steps. We cropped a circle in Fiji to remove the reconstruction artifacts on the edge of the 3D volume. The outside was afterwards manually set to the value 0 (black). Black slices with no information on the top and the bottom were removed and the different time steps were taken apart again. The images were then ready to run with the digital volume correlation algorithm.

The .tif images were eventually loaded into MatLab and saved as .mat files. With these files, the fast iterative digital volume correlation algorithm for large deformations (FIDVC) was run. [23] The calculated results were then exported as .vtk files and visualized in Paraview. [24] To convert the output file from pixels to displacement, we multiplied the data by 4 (downsizing) and by 0.1625 µm/pix (resolution).

2.5. Indentation

Samples for indentation experiments were cold sintered prior to the testing. To this end, 0.3 g of particles were mixed with 0.075 ml of DI water, poured into a pressing tool (Modell 10, Gr. 2, diameter 11 mm, P/O Weber, Germany) and pressed at 500 MPa for 1 hour using a mechanical testing machine (Instron 8562, Instron). The resulting pellets were 87 % dense. The pellets were fixed onto the stage for indentation using a wax. The indentation was performed in a NanoTest Vantage from Micro Mechanics (Wrexham, U.K.) using a Berkovich tip. For the microindents, the force was increased with a speed of 80 mN s^{-1} until a holding force of 4800 mN was reached. The sample was then unloaded with the same speed. For the nanoindents, we programmed the instrument to perform an array of 100 indents (10 by

10). In this case, the force was increased with a speed of 0.25 mN s^{-1} until the holding force of 5 mN was reached. The sample was unloaded with the same speed. Specimens measured under wet conditions were soaked in water prior to the test. A wet sponge was attached next to these samples to minimize water evaporation during the measurement.

3. Results and discussion

3.1. Multiscale spatial and temporal analysis of the cold sintering process

Vaterite compacts that undergo cold sintering exhibit a multiscale structure, consisting of an assembly of interconnected nanoparticles inside individual agglomerates and the assembly of agglomerates into a macroscopic sample of well-defined geometry (Fig. 1 top row). The deformation of the assembly of nanoparticles and the assembly of agglomerates under the imposed uniaxial stress determines the creep rate, the final relative density, and the possible build-up of density gradients within the compacts. To shed light on the contribution of these multiscale deformation processes on the cold sintering of vaterite compacts we employ *in-situ* X-Ray tomography during uniaxial pressing and instrumented mechanical indentation on compacted samples at two different length scales (Fig. 1 bottom row). *In-situ* X-Ray tomography was used to quantify the deformation of agglomerates throughout the mechanically-loaded compact by measuring the evolution of local displacement in stress relaxation experiments. Instrumented mechanical indentations were performed on compacted specimens to measure the deformation of the assembly of nanoparticles and of the assembly of agglomerates at the micro- and nano-scales, respectively, and their contributions to the overall creep rate of the macroscopic vaterite sample.

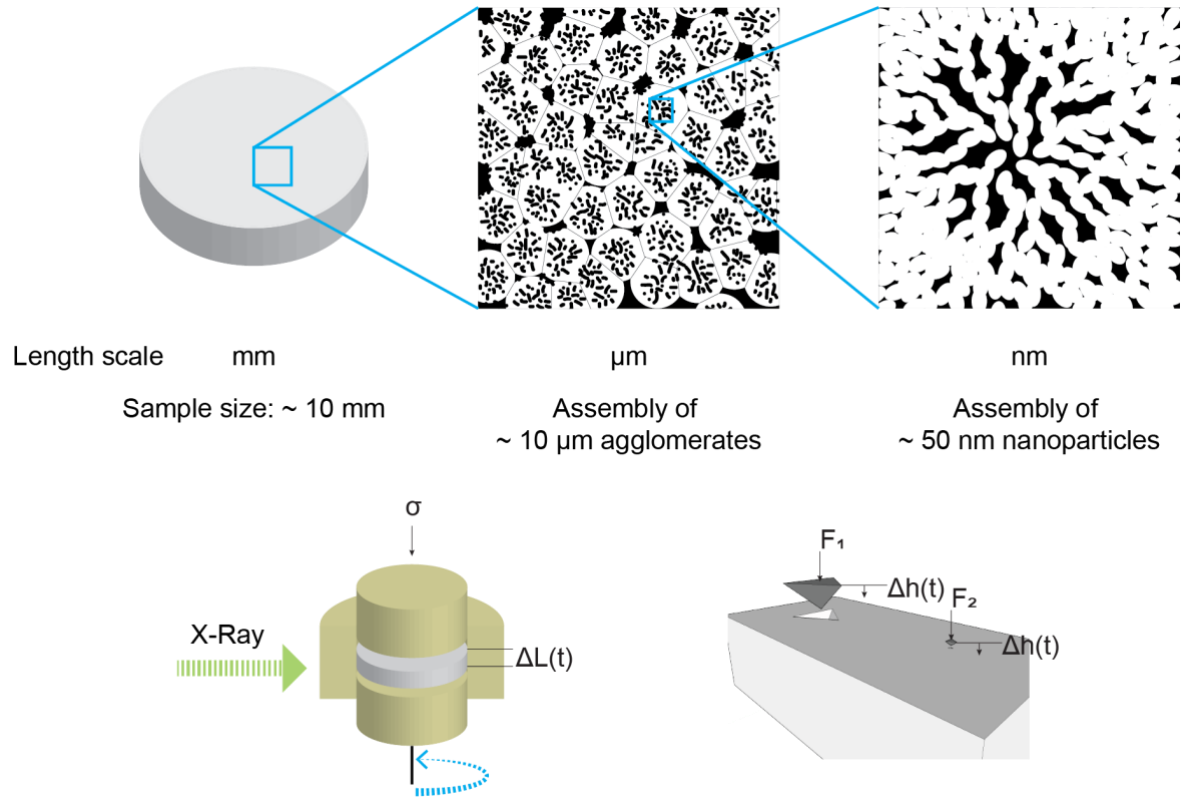

Figure 1: Schematics of the multiscale structure of the nanovaterite compacts and the characterization tools used to study the cold sintering process. Top row: Hierarchical structure of the vaterite compact, indicating (left) the macroscopic sample, (middle) the assembly of micron-sized agglomerates of vaterite nanoparticles, and (right) the network of vaterite nanoparticles inside an agglomerate. Bottom row: multiscale mechanical analysis of the vaterite compacts using (left) macroscopic mechanical tests coupled with *in-situ* synchrotron X-Ray tomography, and (right) instrumented indentation at the micro- and nanoscale.

Specimens for these experiments were prepared from nanovaterite powder obtained from the precipitation of calcium chloride and sodium carbonate in water, as previously reported. [21] The precipitation reaction results in spherical agglomerates in the size range 8-15 μm, which are formed by interconnected nanoparticles with size on the order of 50 nm (Fig. 2). X-Ray diffraction of the precipitated powder confirms the formation of vaterite crystals. The presence of a calcite peak in the X-Ray diffraction spectrum is associated with the formation of a few large calcite particles that are readily visible by SEM imaging.[21]

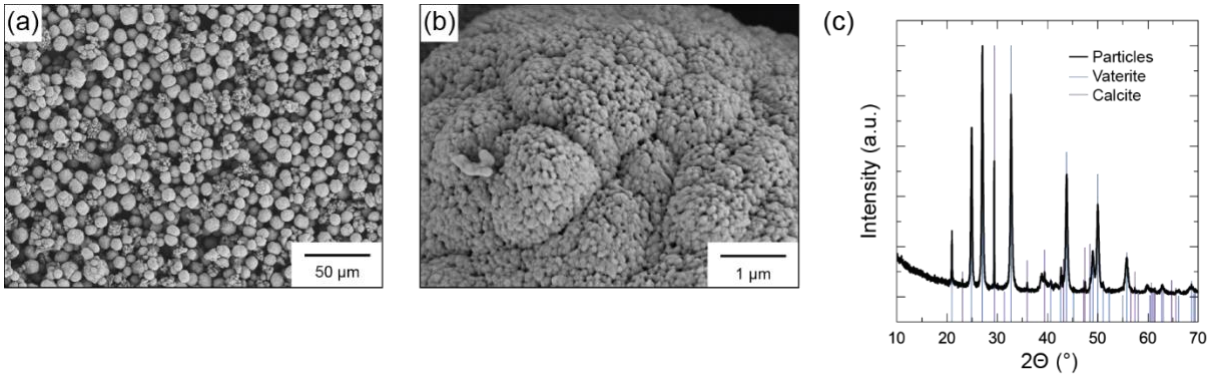

Figure 2: Nanovaterite powder used for the preparation of compacts. (a) Spherical vaterite agglomerates obtained after the precipitation reaction. (b) Hierarchical structure of the vaterite agglomerates, highlighting the presence of interconnected nanoparticles at smaller length scales. (c) X-Ray powder diffraction of the precipitated nanopowder, which indicates the predominant formation of vaterite crystals.

3.2. In situ X-Ray synchrotron tomography

The compaction behavior of the vaterite powder was investigated by performing *in-situ* X-Ray tomography while the sample was subjected to uniaxial die pressing in a custom-made mechanical tester (Fig. 3a,b). To enable the visualization of individual agglomerates, this experimental setup was assembled in a synchrotron light source that provides a pixel size of 162.5 nm and temporal resolution of 0.03 Hz (PSI, Villigen). The vaterite powder was pressed inside a custom-made alumina crucible of 0.50 mm inner diameter with walls that are sufficiently thin to minimize X-Ray attenuation but thick enough to enable compression of the sample under a uniaxial stress of up to 500 MPa (Fig. 3c, d). By rotating the cylindrical sample around its long axis during the measurement, three-dimensional reconstructions of the microstructure were first obtained when the targeted pressure was reached. This was followed by tomography measurements 2, 5, 10, 20 and 30 min after the initial scan under external pressure (Fig. 3c). The spatial resolution achieved at the beamline was high enough to visualize the shape of individual particles (Fig. 3d).

Compression experiments were carried out by applying uniaxial pressures of 100 or 500 MPa onto the powder with water (wet) or under dry conditions. This initial pressure was reached by applying a constant displacement rate in the first stage of the compression test. After this maximum pressure was reached, the sample was allowed to relax under the initially imposed displacement (stage 2, Fig. 3c). The results of the compression experiments show a significant effect of the presence of water on the stress relaxation behavior of the vaterite compacts. A stress drop of 40% was observed in the presence of water for samples subjected to an uniaxial pressure of 500 MPa. By contrast, the experiment with dry powder showed a stress drop of only 10% for this initial pressure. A similar trend was found for the specimens subjected to the initial stress of 100 MPa.

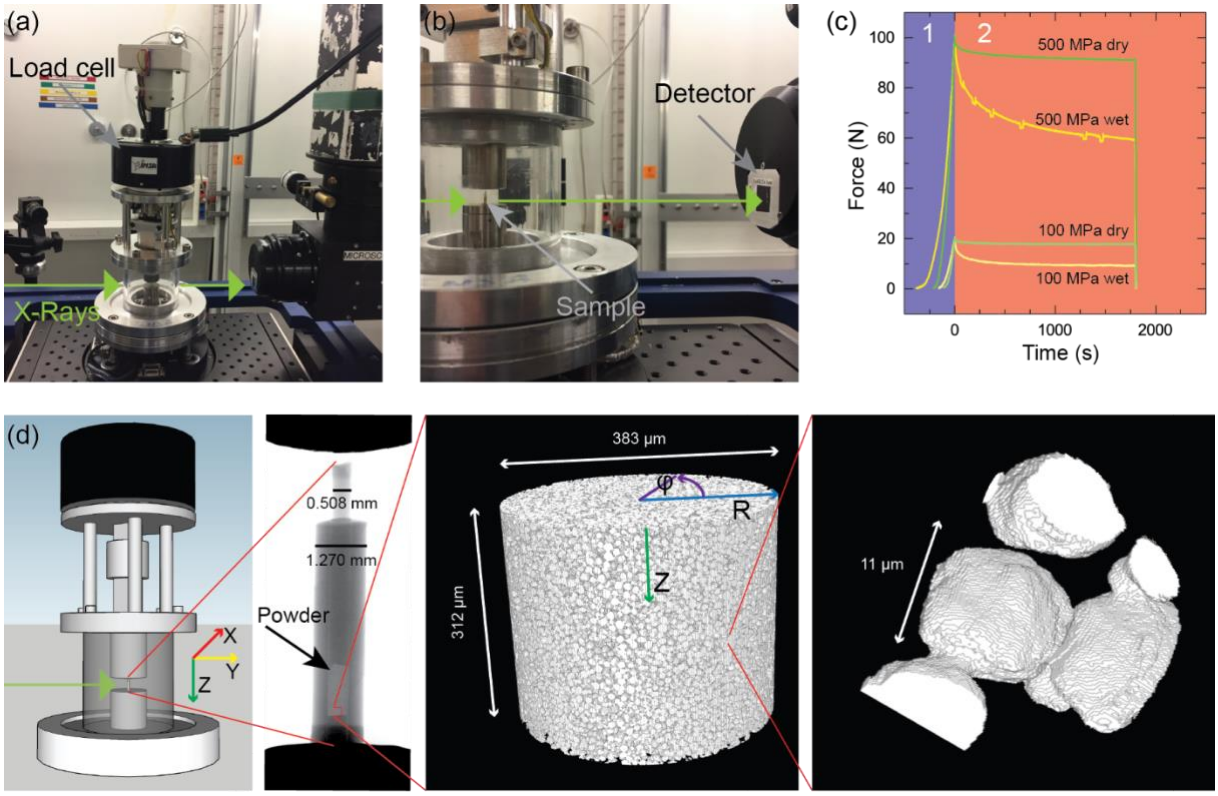

Figure 3: *In-situ* synchrotron X-Ray tomography setup and three-dimensional reconstructed images of a mechanically-tested compact. (a,b) Mechanical testing apparatus positioned in front of an X-Ray beamline at the synchrotron facility. (c) Mechanical compaction (stage 1, blue) and stress relaxation (stage 2, red) curves recorded simultaneously with the *in-situ* X-Ray tomography measurements. (d) Schematic representation of the uniaxial pressing tool under the load cell (left), highlighting the location of the nanovaterite powder inside the custom-made alumina crucible (middle left). The load cell was constructed to fit into the beamline and can rotate freely to acquire all necessary images for the 3D reconstruction. Representative 3D reconstruction of the vaterite compact acquired at the bottom of the pressing tool (middle right), indicating the coordinate system used to describe the compaction process and a representative reconstruction of several nanovaterite agglomerates showing the necks between them (right).

The observed stress relaxation is caused by the deformation of particles and agglomerates within the mechanically-loaded vaterite compact. To quantify the deformation at the length scale of agglomerates, we performed digital volume correlation analysis between tomographic images obtained at 0 min and after 30 min at the end of the stress relaxation experiments (Fig. 4a). The displacement vectors obtained by digital volume correlation provide valuable information about local variations in the relative motion of agglomerates within the sample. To analyze such local variations we map the length of the displacement vector along the Z direction using 2D vertical slices of the reconstructed tomograms (Fig. 4b). Longitudinal displacements at selected radial positions at the center and edges of the reconstructed tomograms are then plotted as a function of the sample height to quantitatively compare the deformation of the compact under different testing conditions (Fig. 4c).

The resulting plots show that a clear negative displacement gradient develops along the height (z) of the compacts tested in water, whereas dry samples display a less-defined displacement profile in the z direction with even a positive gradient in the bottom half of the pressing tool. The negative displacement

gradient measured for the wet samples indicates the development of strong compressive strains inside the compact along the pressing direction. For samples subjected to an external stress of 500 MPa, the displacements are 10-fold higher than those measured for specimens tested in the dry state under the same pressure. This shows that the presence of water clearly promotes the densification of the compact through the longitudinal displacement of vaterite agglomerates. Such longitudinal displacement arises most likely from deformation processes at the contact points between agglomerates, which change their initial spherical morphology into more densely packed truncated shapes. In contrast to the wet compacts, specimens tested in the dry state showed no detectable longitudinal displacement at 100 MPa and a relatively weak compressive longitudinal displacement at 500 MPa. The significant radial (off-axis) displacement observed in these dry specimens (Fig. 4a) suggest that the agglomerates in these compacts undergo lateral rearrangements that do not allow for an effective reduction of the material's internal stresses. Such behavior is typical of brittle powders subjected to uniaxial pressing. [25]

To better quantify the longitudinal compressive strains developed during the cold sintering process with water, we evaluate in more details the displacement gradients formed within the wet specimen pressed at 500 MPa. Longitudinal strains ϵ_z are directly obtained from the slope of the line fitted to the z displacement value, d_z, when plotted against the height (z) of the sample: $\epsilon_z = \frac{\partial d_z}{\partial z}$. Using this fitting approach, strain data at selected radial positions at the center and edges of the compact were derived from the reconstructed tomographs (Fig. 4c). The slopes of the fitted data show that the wet samples subjected to 500 MPa reach longitudinal strain values as high as 2% and 3% at the edge and close to the center of the compact, respectively. The lower strain at the edge of the compact may result from the friction of the powder that is located closer to the walls of the alumina die. The observed difference in compressive strain leads inevitably to a densification gradient between the center and the edge of the compact. Taking the experimentally-measured relative density of 79% at the beginning of the stress relaxation test, we estimate the relative densities at the center and at the edge of the compact to reach, respectively, 81% and 82% at the end of the experiment.

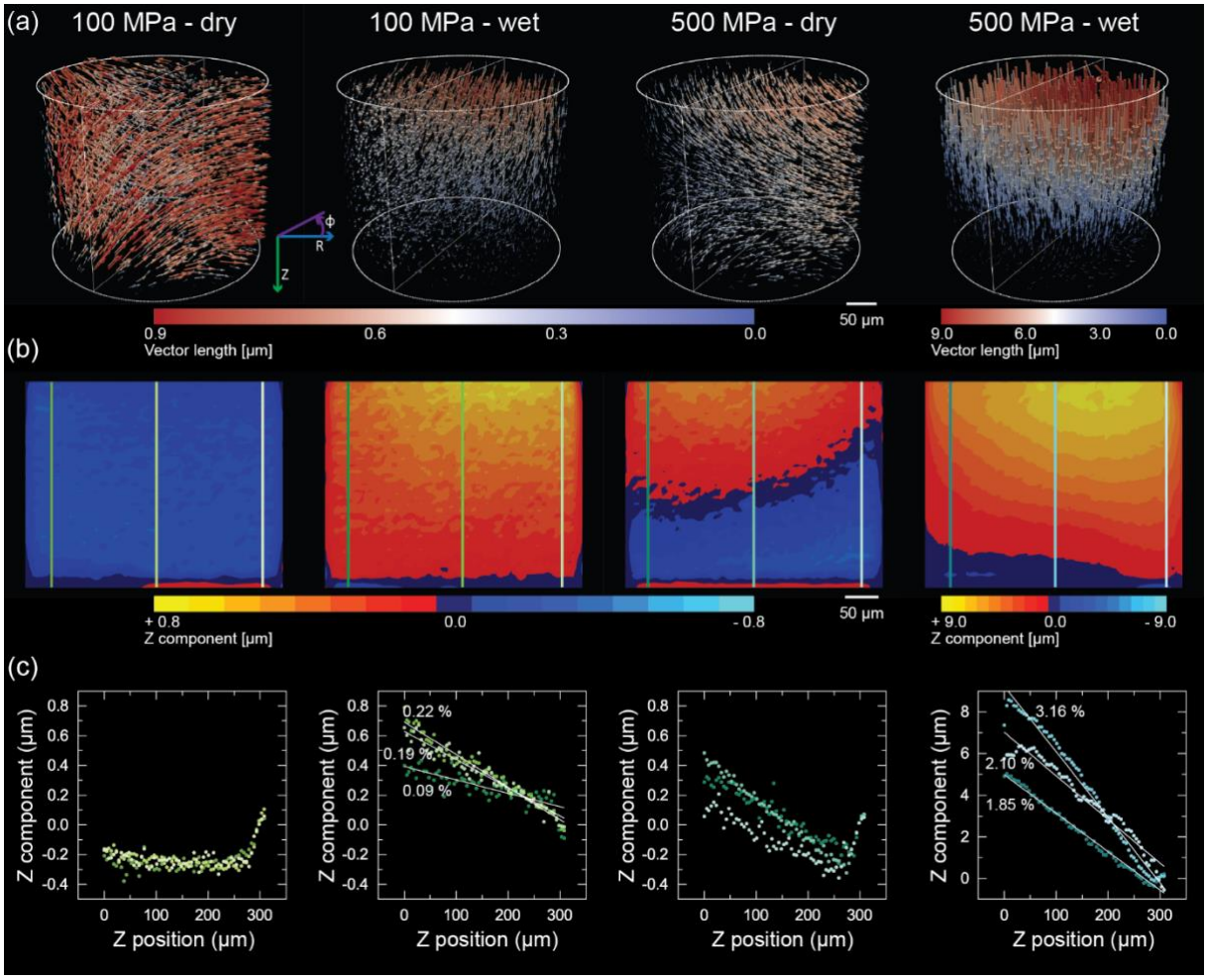

Figure 4: Displacement of agglomerates after stress relaxation of vaterite compacts subjected to distinct mechanical loading conditions. (a) 3D representations of the total displacement vectors indicating the motion of agglomerates inside vaterite compacts initially loaded with 100 or 500 MPa under dry or wet conditions. The displacement vectors were measured by Digital Volume Correlation of image-stacks acquired at the beginning (0 min) and end (30 min) of the stress relaxation experiments. (b) Contour plots displaying the magnitude of agglomerate displacement along the *z* direction for representative vertical slices of the 3D volumes shown in (a). The color code represents the magnitude of the vector component. (c) z-displacement of agglomerates as a function of the sample height for different mechanical testing conditions. The displacement data were obtained along the three different radial positions shown in Fig. 4b. Lines were fitted to the displacement data to estimate the local strain along the edges and center of the compact after stress relaxation.

In addition to the total strain at the end of the densification process, we also use our 3D reconstructed tomographs to assess the evolution of the strain distribution inside the wet compact during stress relaxation (Fig. 5). This provides valuable information about the propagation of the externally imposed stress throughout the compact microstructure. For wet specimens pressed at 500 MPa, the restructured tomographs indicate that most of the longitudinal displacement within the compact develops in the first few couple of minutes of the 30-min long stress relaxation experiment (Fig. 5a,b). Indeed, the net displacement measured after 2 minutes is about 3 times higher than that observed in the last 10 minutes of the test. Such a high initial deformation releases some of the elastic energy stored in the pressed

compact, resulting in the strong stress relaxation detected by the mechanical load cell in the beginning of the test.

Analysis of the cumulative displacement maps at the early stage of the relaxation experiment also indicates that the developed strain is uniform along the entire height of the compact within the first minutes of the test (Fig. 5c,d). The lack of strain gradients within the sample implies the existence of an elastic network of percolating agglomerates, which quickly distributes the externally applied stress through stress transfer at inter-agglomerate contacts (Fig. 3d). Despite the uniform strain distribution along the height of the sample, we found that the expected lower strains at the edge of the compact are already visible at a very early stage of the stress relaxation experiment. This is evident by comparing the estimated strains at the edge and at the center of the specimen as a function of time. Such comparison shows that the strain mismatch remains relatively constant throughout the densification process (Fig. 5d,e). In addition to the increased friction of the powder located closer to the die walls, the observed radial gradient and the asymmetry of the displacement data might also arise from the fact that the pressing punches used in these experiments are not perfectly flat.

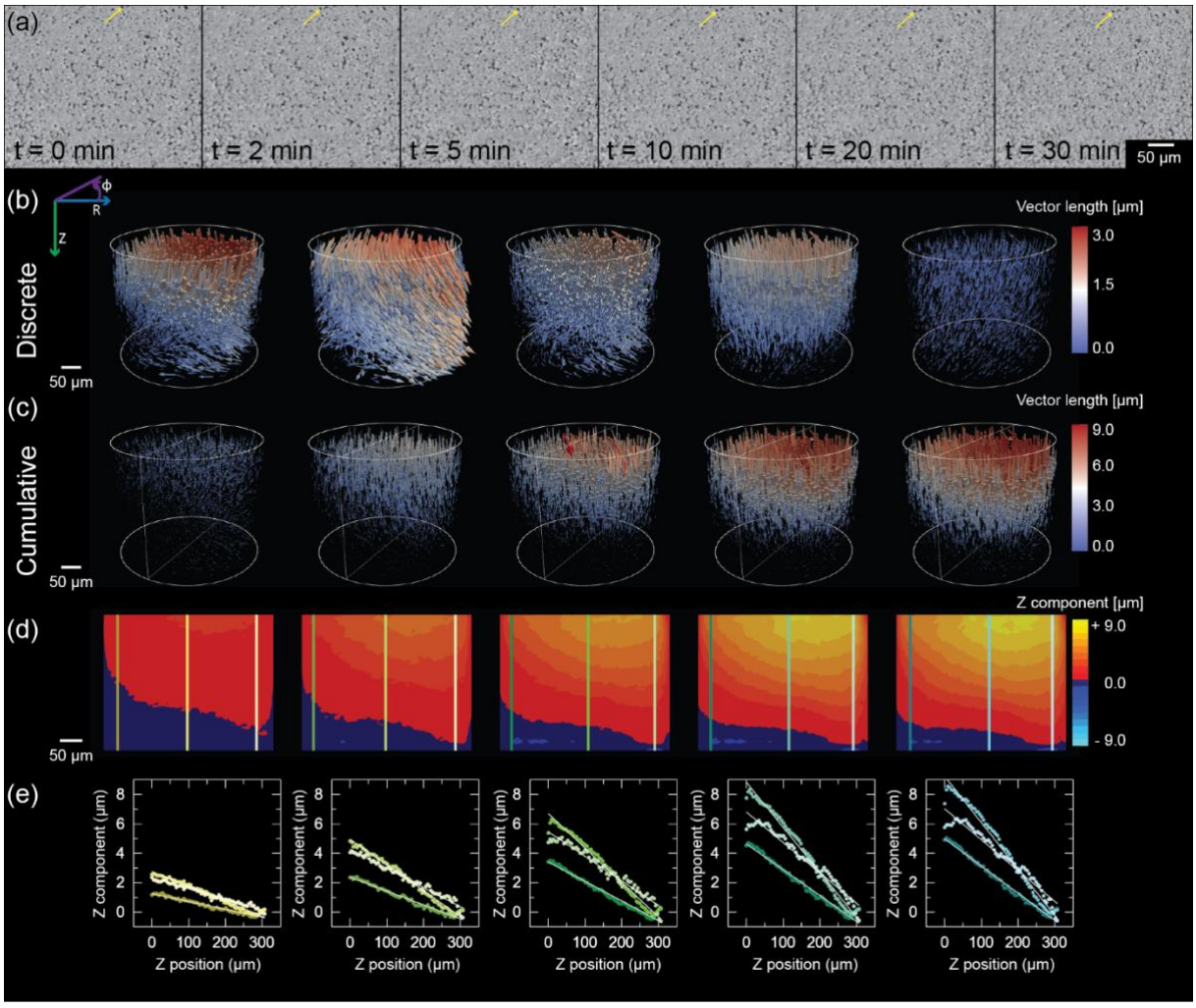

Figure 5: Evolution of the agglomerate displacement during stress relaxation of vaterite compacts initially pressed at 500 MPa with water. (a) Snapshots of the microstructure of the compact

obtained at different time points along the stress relaxation process. The images correspond to vertical slices of 3D tomography reconstructions. The local displacement of agglomerates inside the compact is qualitatively illustrated by tracking a pore positioned close to the top of the specimen (yellow arrow). (b,c) 3D representations of the displacement vectors of agglomerates measured (b) between snapshots or (c) accumulated over the entire stress relaxation experiment. The color code represents the magnitude of the vector. (d) Contour plots displaying the magnitude of agglomerate displacement along the *z* direction for representative vertical slices of the 3D volumes shown in (c). (e) z-displacement of agglomerates as a function of the sample height measured at the edges and center of the compact at selected time points along the test.

3.3. Instrumented micro and nano indentation

Whereas the high longitudinal strains developed within the wet compacts clearly illustrate the strong effect of water on the densification process, elucidating the origin of the observed internal displacements requires further systematic experiments. We address this question by measuring the deformation of the compact at two different length scales using instrumented indentation tools. Indentation tests at the nanoscale are carried out to quantify the deformation of the assembly of nanoparticles within a single agglomerate, whereas measurements at the microscale are conducted to assess the deformation of the assembly of agglomerates at a larger length scale. The experiments were performed under wet or dry conditions by first loading the specimen at a constant force rate, followed by a creep test at a target fixed force (Fig. 6a,d). The evaluated specimen was prepared by cold sintering the nanovaterite powder with water at 500 MPa to obtain a 11mm diameter disc with a final relative density of 87%. Scanning electron microscopy images of imprints generated upon indentation confirm that the selected micro or nano-indenters could be appropriately positioned to probe either the assembly of agglomerates or the assembly of nanoparticles, respectively (Fig. 6c,f). The micro-imprints were typically 100 μm wide and 10 μm deep, whereas the nano-imprints exhibited width of 1 μm and depth of 100 nm. These dimensions are at least 10-fold larger than the average size of a single agglomerate (10 μm) and an individual nanoparticle (50 nm), which validates our experimental protocol as a means to probe the deformation of assemblies of agglomerates and particles at two different length scales.

The creep data obtained from the indentation experiments confirm the crucial effect of water in promoting the densification of the compact under constant mechanical stress (Fig. 6b,e). Samples containing water displayed 4-fold and 2-fold higher displacements compared to the dry counterparts at the end of the nano- and micro-indentation tests, respectively. Comparison of the creep behavior of wet specimens probed at the nano- and microscales allows us to identify the deformation mechanism controlling the densification of the vaterite compacts. Because of the difference in indented volume at the two different length scales, we compare these two samples in terms of the rate at which the specimen changes its creep compliance (*L*) over time. Following a previously reported analytical model, [20] the creep compliance of the sample can be measured from indentation experiments using the equation:

$$L(t) = \frac{2 \cdot tan\,(\theta)}{\pi \cdot P_{max}} \cdot h^2(t), \qquad \text{(Eq. 1)}$$

where θ is the half cone angle of the Berkovich indenter used in the experiments (65.3°), P_{max} is the maximum load, and $h(t)$ is the actual indentation depth at a given time t. After calculating the time-

dependent compliance of the sample from the indentation depth data, the resulting creep compliance curves were differentiated with respect to time to determine the creep compliance rate (*dL(t)/dt*) of specimens at the micro- and nano-scales (Fig. 6g,h). [20]

Our analysis reveals that the creep compliance rate of the wet vaterite compact is approximately twice larger than that of the dry specimen over the entire time window of the experiments. Importantly, we found that the creep compliance rate of samples tested with a nano-indenter display similar or even slightly higher levels compared to the rate measured with the micro-indenter. This indicates that the creep response of the compact is predominantly controlled by the deformation of the assembly of nanoparticles inside an individual agglomerate. Indeed, if the relative displacement between the agglomerates were to play a role in the creep process, this would be reflected in a higher creep compliance rate of samples tested by micro-indentation.

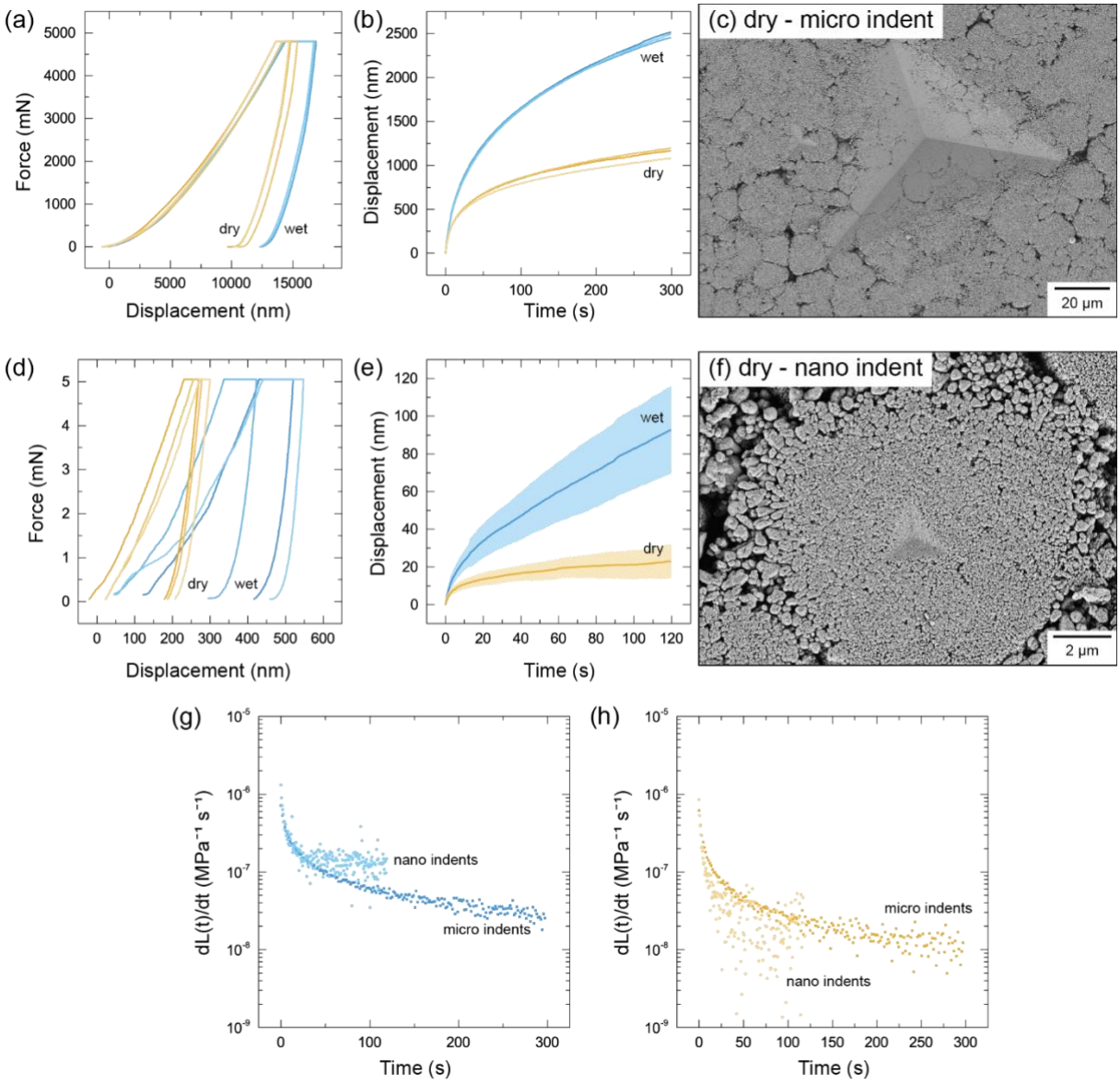

Figure 6: **Multiscale creep of vaterite compacts measured by mechanical indentation at the nano- and microscales.** (a,d) Force-displacement curves obtained from (a) micro- and (d) nano-indentation experiments performed on a vaterite sample that was previously cold sintered to reach 87% relative density. (b,e) Displacement of the indenter as a function of time obtained from creep tests under constant load at (b) the micro- and (e) the nano-scales. The curves in (e) indicate the average displacement, whereas the shaded areas represent the standard deviation. (c,f) Scanning electron microscopy images depicting the imprints generated on the surface of vaterite specimens after (c) micro- and (f) nano-indentation experiments in dry conditions. (g,h) Evolution of the creep compliance rate ($dL(t)/dt$) over time for vaterite compacts tested by micro- and nano-indentation in (g) wet or (h) dry conditions.

Such experimental results suggest that the densification process of the vaterite compacts with water at constant mechanical load ultimately results from the deformation of the assembly of nanoparticles at the contact points between individual agglomerates. This intra-agglomerate deformation at the contact points should lead to truncated geometries of higher packing density, thus increasing the relative density of the entire compact. Because of the stress intensification effect at the contact points between agglomerates, the hierarchical nature of the vaterite nanopowder is expected to favor the densification of the compact by amplifying the external stresses at inter-agglomerate contacts while also providing a network of nanoparticles that can be effectively densified inside the individual agglomerates.

Overall, our analysis suggests that the densification of the vaterite compacts is controlled by localized deformation processes operating over three distinct length scales. At the scale of the pressing die, frictional forces and imperfections of the punch seem to favor the deformation of powder in the center of the compact. In turn, stress intensification at inter-agglomerate contacts promotes localized deformation of specific sites at the length scale of individual agglomerates. Eventually, the assembly of interconnected nanoparticles at the smallest length scale undergoes the actual deformation required for the macroscopic densification of the compact.

5. Conclusions

The cold sintering of nanovaterite powder via uniaxial pressing with water involves deformation processes that operate at multiple length scales. Tomography imaging performed at scales much larger than individual agglomerates show that high uniaxial compressive strains develop within compacts containing water. This enables strong densification along the loading direction for powders subjected to stress relaxation under wet conditions. By contrast, dry pressing leads to predominantly lateral motion of the agglomerates and therefore weak densification along the pressing direction. Because lower compressive strains are achieved closer to the walls of the pressing die, a small difference in relative density between the center and the edges of compact is observed. Snapshots taken during stress relaxation experiments suggest that the vaterite agglomerates form a percolating network that quickly transmits the applied external stresses throughout the powder compact. This indicates that densification under constant mechanical load likely initiates at the contact points between the vaterite agglomerates. The high stresses developed at such contact points irreversibly deforms the network of interconnected nanoparticles inside individual agglomerates, which become truncated and more closely packed within the compact. The irreversible deformation of the nanoparticle network within each agglomerate

ultimately controls the densification rate of the entire compact. This implies that possible agglomerate rearrangement events occur predominantly in the initial loading stage of the pressing operation, leaving further gains in densification to the deformation of the nanoparticles inside agglomerates. Our experimental study provides important insights onto the effect of water and powder morphology on the room-temperature cold sintering of nanovaterite and may help identify novel powders amenable to this environmental-friendly manufacturing technology.

Acknowledgements

We thank Dr. Marta Gallo for her help during our beam time at PSI, Dr. Samuel Humphry-Baker for his support with the indenter at Imperial College and Dr. Thomas Weber from the X-Ray Platform of the Department of Materials (ETH Zurich) for his help with the XRD measurements. We are also thankful to Dr. Alessandro Ofner for the access to the workstation from Microcaps AG to perform the DVC calculations. The Swiss National Science Foundation (consolidator grant BSCGIO_157696) is also gratefully acknowledged for financing this research.

References

[1] P. De Silva, L. Bucea, V. Sirivivatnanon, D.R. Moorehead, Carbonate binders by “cold sintering” of calcium carbonate, J. Mater. Sci. 42(16) (2007) 6792-6797.

[2] J.-P. Gratier, D.K. Dyshe, F. Renard, Chapter 2 - The Role of Pressure Solution Creep in the Ductility of the Earth’s Upper Crust, ADV GEOPHYS 54 (2013) 47-179.

[3] F. Bouville, A.R. Studart, Geologically-inspired strong bulk ceramics made with water at room temperature, Nat. Commun. 8 (2017) 14655.

[4] B. Dargatz, J. Gonzalez-Julian, O. Guillon, Improved compaction of ZnO nano-powder triggered by the presence of acetate and its effect on sintering, Sci. Technol. Adv. Mater. 16(2) (2015) 025008.

[5] H. Kähäri, M. Teirikangas, J. Juuti, H. Jantunen, Dielectric Properties of Lithium Molybdate Ceramic Fabricated at Room Temperature, J. Am. Ceram. Soc. 97(11) (2014) 3378-3379.

[6] J. Guo, H. Guo, A.L. Baker, M.T. Lanagan, E.R. Kupp, G.L. Messing, C.A. Randall, Cold Sintering: A Paradigm Shift for Processing and Integration of Ceramics, Angew. Chem. Int. Ed. 55(38) (2016) 11457-11461.

[7] X. Zhang, C.J. Spiers, Compaction of granular calcite by pressure solution at room temperature and effects of pore fluid chemistry, Int. J. Rock Mech. Min. Sci. 42(7-8) (2005) 950-960.

[8] J. Gonzalez-Julian, K. Neuhaus, M. Bernemann, P.J. da Silva, A. Laptev, M. Bram, O. Guillon, Unveiling the mechanisms of cold sintering of ZnO at 250 °C by varying applied stress and characterizing grain boundaries by Kelvin Probe Force Microscopy, Acta Mater. 144 (2018) 116-128.

[9] J. Guo, R. Floyd, S. Lowum, J.-P. Maria, T.H.d. Beauvoir, J.-H. Seo, C.A. Randall, Cold Sintering: Progress, Challenges, and Future Opportunities, Annu. Rev. Mater. Res. 49(1) (2019) 275-295.

[10] P.K. Weyl, Pressure solution and the force of crystallization: a phenomenological theory, J. Geophys. Res. 64(11) (1959) 2001-2025.

[11] D. Grossin, S. Rollin-Martinet, C. Estournès, F. Rossignol, E. Champion, C. Combes, C. Rey, C. Geoffroy, C. Drouet, Biomimetic apatite sintered at very low temperature by spark plasma sintering: Physico-chemistry and microstructure aspects, Acta Biomater. 6(2) (2010) 577-585.

[12] E. Maire, P.J. Withers, Quantitative X-ray tomography, Int. Mater. Rev. 59(1) (2014) 1-43.

[13] O. Lame, D. Bellet, M.D. Michiel, D. Bouvard, In situ microtomography investigation of metal powder compacts during sintering, Nucl. Instrum. Methods Phys. Res., Sect. B 200 (2003) 287-294.

[14] O. Lame, D. Bellet, M. Di Michiel, D. Bouvard, Bulk observation of metal powder sintering by X-ray synchrotron microtomography, Acta Mater. 52(4) (2004) 977-984.

[15] E. Maire, C. Le Bourlot, J. Adrien, A. Mortensen, R. Mokso, 20 Hz X-ray tomography during an in situ tensile test, Int. J. Fract. 200(1) (2016) 3-12.

[16] A. Nommeots-Nomm, C. Ligorio, A.J. Bodey, B. Cai, J.R. Jones, P.D. Lee, G. Poologasundarampillai, Four-dimensional imaging and quantification of viscous flow sintering within a 3D printed bioactive glass scaffold using synchrotron X-ray tomography, Materials Today Advances 2 (2019) 100011.

[17] Z. Yan, O. Guillon, C.L. Martin, S. Wang, C.-S. Lee, F. Charlot, D. Bouvard, Correlative Studies on Sintering of Ni/BaTiO3 Multilayers Using X-ray Computed Nanotomography and FIB-SEM Nanotomograhy, J. Am. Ceram. Soc. 98(4) (2015) 1338-1346.

[18] F. Renard, D. Bernard, X. Thibault, E. Boller, Synchrotron 3D microtomography of halite aggregates during experimental pressure solution creep and evolution of the permeability, Geophys. Res. Lett. 31(7) (2004).

[19] W.C. Oliver, G.M. Pharr, An improved technique for determining hardness and elastic modulus using load and displacement sensing indentation experiments, J. Mater. Res. 7(6) (1992) 1564-1583.

[20] M. Vandamme, C.A. Tweedie, G. Constantinides, F.-J. Ulm, K.J. Van Vliet, Quantifying plasticity-independent creep compliance and relaxation of viscoelastoplastic materials under contact loading, J. Mater. Res. 27(1) (2011) 302-312.

[21] B.V. Parakhonskiy, A. Haase, R. Antolini, Sub-Micrometer Vaterite Containers: Synthesis, Substance Loading, and Release, Angew. Chem. Int. Ed. 51(5) (2012) 1195-1197.

[22] J. Schindelin, I. Arganda-Carreras, E. Frise, V. Kaynig, M. Longair, T. Pietzsch, S. Preibisch, C. Rueden, S. Saalfeld, B. Schmid, J.-Y. Tinevez, D.J. White, V. Hartenstein, K. Eliceiri, P. Tomancak, A. Cardona, Fiji: an open-source platform for biological-image analysis, Nat. Methods 9(7) (2012) 676-682.

[23] E. Bar-Kochba, J. Toyjanova, E. Andrews, K.-S. Kim, C. Franck, A Fast Iterative Digital Volume Correlation Algorithm for Large Deformations, Experimental Mechanics 55(1) (2015) 261-274.

[24] J. Ahrens, B. Geveci, C. Law, ParaView: An End-User Tool for Large Data Visualization, Visualization Handbook (2005).

[25] M.N. Rahaman, Ceramic Processing and Sintering, 2 ed., CRC Press2003.